



# Improved Multicomponent Multiphase Lattice Boltzmann Model for Physical Foaming Simulation

G. Lin, C. Geng, L. Zhang and F. liu<sup>†</sup>

*College of Electromechanical Engineering, Qingdao University of Science & Technology, Qingdao, Shandong Province, 266061, China*

<sup>†</sup>Corresponding Author Email: [liufumin@qust.edu.cn](mailto:liufumin@qust.edu.cn)

(Received February 18, 2022; accepted April 18, 2022)

## ABSTRACT

The lattice Boltzmann models, especially the pseudopotential models, have been developed to investigate multicomponent multiphase fluids in presence of phase change process. However, the interparticle force between different components causes compressibility error in the non-phase-change component. This restricts the model capability in quantitative analysis of the physical foaming process, such as expansion rate and decay time. In the present study, a multicomponent multiphase pseudopotential phase change model (the MMPPCM) is improved by introducing an effective mass form of high-pressure-difference multicomponent model in the non-phase-change component. The improved model is compared with the MMPPCM based on simulations of the phase change process of static and moving fluids, as well as the physical foaming process. Density variation of non-phase-change component and its effect on flow field characteristics are analyzed during the phase change process. Simulation results of physical foaming process lead to about 10% ~ 20% reduction of the compressibility error for the improved model as compared with the results of MMPPCM. The improved model also enhances the computational stability of phase change simulation of the static droplets.

**Keywords:** Lattice Boltzmann method; Multicomponent; Multiphase; Physical foaming; Compressibility error.

## NOMENCLATURE

$a$	a parameter in Peng–Robinson equation of state	$R$	a parameter in Peng–Robinson equation of state
$b$	a parameter in Peng–Robinson equation of state	$\mathbf{r}$	lattice site
$c_0$	a parameter in interparticle force function	$r_i$	initial radius of droplets
$c_s$	speed of sound in lattice unit	$T$	temperature
$c_v$	specific heat capacity	$T_c$	critical temperature
$\mathbf{e}_\alpha$	discrete velocity along $\alpha$ direction	$T_{\text{wall}}$	wall temperature
$\mathbf{F}$	body force	$t$	time
$\mathbf{F}_g$	gravitational force	$t_d$	bubble departure time
$\mathbf{F}_{\sigma,\text{int}}$	interparticle force	$\mathbf{u}$	macroscopic velocity
$f(x)$	function for calculating the number of droplets	$\mathbf{u}_\sigma$	macroscopic velocity of the component $\sigma$
$f_{\sigma,\alpha}$	density distribution function of the component $\sigma$ along $\alpha$ direction	$v$	velocity magnitude
$f_{\sigma,\alpha}^{\text{eq}}$	density equilibrium distribution function of the component $\sigma$ along $\alpha$ direction	$w_{\sigma,\alpha}$	weight coefficient for discrete velocity
$\mathbf{G}$	gravity vector	$X$	number of lattice sites in a computation domain
$g_{\sigma\bar{\sigma}}$	a parameter describing the strength of the interaction force	$x$	area of a single droplet (bubble) in the function for calculating the number of droplets
$H_{\text{ave}}$	average liquid level	$Y$	$Y$ coordinates
$h_\alpha$	temperature distribution function along $\alpha$ direction	$\gamma$	surface tension
$h_\alpha^{\text{eq}}$	temperature equilibrium distribution	$\Delta f_{\sigma,\alpha}$	source term in density evolution equation
		$\delta_t$	time step
		$\lambda$	thermal conductivity
		$\rho$	density
		$\rho_{\text{ave}}$	average density

	function along $\alpha$ direction	$\rho_\sigma$	density of the component $\sigma$
$i$	a parameter in effective mass function of the improved model	$\tau_T$	dimensionless relaxation time for temperature
$j$	a parameter in effective mass function of the improved model	$\tau_\sigma$	dimensionless relaxation time for density of the component $\sigma$
$k$	a parameter in effective mass function of the improved model	$\phi$	source term in temperature evolution equation
$m$	distribution parameter in the function for calculating the number of droplets	$\chi$	thermal diffusivity
$P$	pressure	$\psi_\sigma$	effective mass of the component $\sigma$
$P_c$	critical pressure	$\omega$	an acentric factor in Peng–Robinson equation of state

## 1. INTRODUCTION

Phase change of one component of multicomponent fluids leads to physical foaming process as a common engineering application, such as foamed asphalt production (Iwański *et al.*, 2021; Li *et al.*, 2020). Because of complex heat and mass transfer, mechanisms, as well as diverse component-phase interactions, numerical analysis of the physical foaming process is challenging. Accordingly, few studies have been conducted in this scope based on conventional computational fluid dynamics (CFD) methods.

In recent years, lattice Boltzmann method (LBM) as a particle-based discrete fluid simulation method has attracted more and more attention (Aliu *et al.*, 2020). In contrast to traditional CFD methods that solve the continuum-based Navier-Stokes equations, LBM solves the Boltzmann equation and considers the collision and streaming processes of mesoscopic particle clusters to describe macroscopic hydrodynamic behavior. Due to microscopic perspective and mesoscopic characteristics, LBM is beneficial in simulation of complex flows such as multiphase multicomponent flow (Xing *et al.*, 2021; Fogliatto *et al.*, 2019), flow in porous media (Jourabian *et al.*, 2012; Zhang *et al.*, 2020), and thermal flow (Lu *et al.*, 2020).

Numerous lattice Boltzmann models have been employed in simulation of single-component multiphase fluids. One of them is the free surface model (Körner *et al.*, 2005), which reduces a two-phase flow problem to a single-phase flow problem. Although this model has been successfully applied in multiphase foaming simulations (Ataei *et al.*, 2021), it is restricted to two-phase flow without phase change process. Other multiphase multicomponent models can be categorized into the color-gradient model (Gunstensen *et al.*, 1991), the pseudopotential model (Shan and Chen, 1993), and the free-energy model (Swift *et al.*, 1996). Among them, the pseudopotential model has been developed into a very popular model (Petersen and Brinkerhoff 2021). This model presumes a non-local interaction between different components (or phases) to resolve phase separation automatically. Although the pseudopotential model is very simple, it involves the basic characteristics of non-ideal fluid flow, namely the equation of state (EOS) and the surface tension. Yuan and Schaefer (2006) introduced a variety of thermodynamic non-ideal

gas state equations into the pseudopotential model to provide a deeper thermodynamic foundation and a reference for subsequent multiphase phase transition research.

Phase change process accompanying with heat transfer in single-component fluids has been investigated by introducing thermal models into the pseudopotential multiphase model. Házi and Márkus (2009) adopted the double distribution function method to define a new pseudopotential function and simulate phase transition. Márkus and Házi (2011) used their model to study phenomena such as plate boiling and evaporation have been studied based on their model. Gong and Cheng (2012) improved Házi’s model (Házi and Márkus, 2009) by considering an extra phase change source term in the passive scalar model to describe the energy change in the boiling process. They also studied generation, growth, and separation processes of bubble during boiling based on this model (Gong and Cheng, 2013; Gong and Cheng, 2015). It has been a popular model in the literature due to good computational stability. However, the above-mentioned LBM-based phase change models mainly focus on single-component multiphase flows.

Regarding phase change process in multicomponent multiphase flows, Li *et al.* (2017) proposed a multicomponent multiphase lattice Boltzmann model to simulate droplets condensation in the presence of non-condensable gas. Zhang *et al.* (2017) developed their own single component phase change model for multicomponent simulation. Zheng *et al.* (2019) developed a multicomponent multiphase thermal lattice Boltzmann model considering vapor-liquid phase change to simulate single droplet condensation in the presence of non-condensable gas. Liu *et al.* (2018) also proposed a multicomponent phase change model, termed as MMPPCM, relying on the single component phase change model (Gong and Cheng, 2012). They simulated phase change process of static and dynamic droplets under gravitational effects. However, because of compressibility of non-phase-change components and computational instability, few models have been used for foaming process research. Except the MMPPCM, the non-phase-change components in the above-mentioned models are limited to the gas. Liu and Wang (2018) simulated physical foaming process based on the MMPPCM, though the results were analyzed

qualitatively due to existence of considerable compressibility.

The present study introduces a high-pressure-difference multicomponent model's effective mass form in the non-phase-change component in order to reduce the compressibility error of Liu's MMPPCM (Liu *et al.*, 2018). The paper is organized as follows. Section 2 first describes the MMPPCM and investigates the reasons for existence of compressibility error, and then presents the improved model. In section 3, the MMPPCM is first verified. This follows by validation of surface tension of the improved model based on simulation of static droplets in binary fluids. Section 4 presents the results obtained by simulation of phase change processes of static and moving fluids, as well as foaming process with orderly distributed droplets. Both of the improved model and the MMPPCM are utilized to confirm the incompressibility improvement. This section also presents simulation results of physical foaming process with randomly distributed droplets and bubbles in order to show capability of the improved model in simulation of the actual foaming process. Section 5 presents the concluding remarks.

## 2. METHODOLOGY

In this section, the MMPPCM is first introduced. The compressibility error in phase change process of this model is then analyzed, and the improved model is finally investigated.

### 2.1 The MMPPCM model

The MMPPCM is proposed based on phase change model of Gong and Cheng (2012) as well as the multicomponent pseudopotential model. The standard lattice Bhatnagar–Gross–Krook equation adopted in the MMPPCM is expressed as follows:

$$f_{\sigma,\alpha}(\mathbf{r}+\mathbf{e}_\alpha\delta_t,t+\delta_t)-f_{\sigma,\alpha}(\mathbf{r},t)=-\frac{1}{\tau_\sigma}(f_{\sigma,\alpha}(\mathbf{r},t)-f_{\sigma,\alpha}^{eq}(\mathbf{r},t))+\Delta f_{\sigma,\alpha}(\mathbf{r},t) \quad (1)$$

where  $f_{\sigma,\alpha}(\mathbf{r},t)$  is the density distribution function of the component  $\sigma$  along the  $\alpha$  direction at the lattice site  $\mathbf{r}$  and time  $t$ , while  $f_{\sigma,\alpha}^{eq}(\mathbf{r},t)$  indicates the corresponding equilibrium distribution function.  $\tau_\sigma$  denotes the dimensionless relaxation time which is defined as 1.0.  $\Delta f_{\sigma,\alpha}(\mathbf{r},t)$  is the body force source term.  $\mathbf{e}_\alpha$  is the discrete velocity along the  $\alpha$  direction, and  $\mathbf{e}_\alpha\delta_t$  represents in the time step  $\delta_t$ . The D2Q9 model consisting of nine discrete velocity vectors in two dimensions is adopted in all simulations of the present work. Figure 1 depicts the discrete velocity vectors in the D2Q9 model.  $\mathbf{e}_\alpha$  is expressed as follows:

$$\mathbf{e}_\alpha = \begin{cases} (0,0); & \alpha = 0; \\ (1,0),(0,1),(-1,0),(0,-1); & \alpha = 1,2,3,4; \\ (1,1),(-1,1),(-1,-1),(1,-1). & \alpha = 5,6,7,8. \end{cases} \quad (2)$$

The equilibrium distribution function  $f_{\sigma,\alpha}^{eq}(\mathbf{r},t)$  is defined as follows:

$$f_{\sigma,\alpha}^{eq} = \rho_\sigma w_{\sigma,\alpha} \left( 1 + \frac{\mathbf{e}_{\sigma,\alpha} \cdot \mathbf{u}_\sigma}{c_s^2} + \frac{(\mathbf{e}_{\sigma,\alpha} \cdot \mathbf{u}_\sigma)^2}{2c_s^4} - \frac{\mathbf{u}_\sigma^2}{2c_s^2} \right) \quad (3)$$

where  $c_s$  is the sound speed in the lattice unit which is  $1/\sqrt{3}$ , and  $w_{\sigma,\alpha}$  is the weight coefficient for each discrete velocity vector given by  $w_0 = 4/9$ ,  $w_{1-4} = 1/9$  and  $w_{5-8} = 1/36$ . The density and velocity of component  $\sigma$  are defined as follows:

$$\rho_\sigma = \sum_\alpha f_{\sigma,\alpha} \quad (4)$$

$$\mathbf{u}_\sigma = \frac{1}{\rho_\sigma} \sum_\alpha f_{\sigma,\alpha} \mathbf{e}_{\sigma,\alpha} \quad (5)$$

Furthermore, the total density and macroscopic velocity of the multicomponent fluids are expressed as follows:

$$\rho = \sum_\sigma \sum_\alpha f_{\sigma,\alpha} \quad (6)$$

$$\mathbf{u} = \sum_\sigma \frac{\rho_\sigma \mathbf{u}_\sigma}{\tau_\sigma} / \sum_\sigma \frac{\rho_\sigma}{\tau_\sigma} \quad (7)$$

The force source term  $\Delta f_{\sigma,\alpha}(\mathbf{r},t)$  is defined using exact-difference-method force scheme (Kupershtokh *et al.* 2009) which is expressed as follows:

$$\Delta f_{\sigma,\alpha}(\mathbf{r},t) = f_{\sigma,\alpha}^{eq}(\rho_\sigma(\mathbf{r},t), \mathbf{u} + \Delta \mathbf{u}) - f_{\sigma,\alpha}^{eq}(\rho_\sigma(\mathbf{r},t), \mathbf{u}) \quad (8)$$

where  $\Delta \mathbf{u} = \mathbf{F} \delta_t / \rho$  indicates the change of velocity induced by the body force during  $\delta_t$ , and  $\mathbf{F}$  is calculated as follows:

$$\mathbf{F} = \mathbf{F}_g(\mathbf{r}) + \mathbf{F}_{\sigma,\text{int}}(\mathbf{r}) \quad (9)$$

where  $\mathbf{F}_g$  is the gravitational force, and  $\mathbf{F}_{\sigma,\text{int}}$  is the interparticle force including both the interaction between different components and the interaction between particles of the same fluid component. These forces are defined as follows:

$$\mathbf{F}_g(\mathbf{r}) = \mathbf{G} \cdot (\rho(\mathbf{r}) - \rho_{ave}) \quad (10)$$

$$\mathbf{F}_{\sigma,\text{int}}(\mathbf{r}) = -c_0 \psi_\sigma(\mathbf{r}) \sum_\sigma g_{\sigma\sigma}(\mathbf{r}, \mathbf{r}') \nabla \psi_\sigma(\mathbf{r}') \quad (11)$$

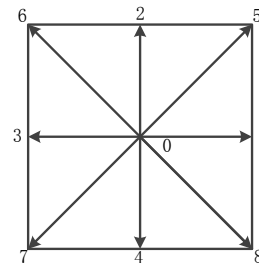


Fig. 1. Discrete velocity vectors in D2Q9 model.

where  $\mathbf{G}$  is the gravitational acceleration vector and  $\rho_{ave}$  is the average density of the multicomponent fluid, such that  $\rho_{ave} = (\sum_X \rho(\mathbf{r})) / X$  for a

computational domain consisting of  $X$  lattice sites. In Eq. (11),  $c_0 = 6.0$  and  $g_{\sigma\bar{\sigma}}$  is a parameter describing the strength of the interparticle force, where  $\sigma = \bar{\sigma}$  for the interaction between particles of the same fluid component, and  $\sigma \neq \bar{\sigma}$  for the interaction between different components. The sign of  $g_{\sigma\bar{\sigma}}$  indicates the interaction force direction, such that the positive and negative signs mean repulsive and attractive forces, respectively. The current study only considers the interaction between neighbor sites.  $g_{\sigma\bar{\sigma}}$  is expressed as follows:

$$g_{\sigma\bar{\sigma}}(\mathbf{r}, \mathbf{r}') = \begin{cases} g_1, & |\mathbf{r} - \mathbf{r}'| = 1; \\ g_2, & |\mathbf{r} - \mathbf{r}'| = \sqrt{2}; \\ 0, & \text{else.} \end{cases} \quad (12)$$

In Eq. (11),  $\psi_\sigma(\mathbf{r})$  is the effective mass which can be defined as a function of  $\rho_\sigma(\mathbf{r})$ . Its gradient, i.e.  $\nabla\psi_\sigma(\mathbf{r})$ , can be calculated by central second-order finite-difference method. Wetting boundary is implemented according to [Martys and Chen \(1996\)](#). It should be noted that the fluid–solid interaction strength is set to be zero in this paper. Accordingly, the contact angle of each fluid is considered to be  $90^\circ$  ([Sedahmed \*et al.\*, 2022](#)).

The present study analyzes the phase change only in a binary fluid consisting of one phase change component (the component 1) and one non-phase-change component (the component 2). Therefore, density of the component 2 is not affected by temperature change in simulations, and the effective mass  $\psi_2(\mathbf{r})$  is expressed as follows:

$$\psi_2(\mathbf{r}) = \rho_2(\mathbf{r}) \quad (13)$$

For the component 1,  $\psi_1(\mathbf{r})$  is calculated as follows:

$$\psi_1(\mathbf{r}) = \sqrt{\frac{2(P_1(\mathbf{r}) - c_s^2 \rho_1(\mathbf{r}))}{c_0 g_{11}(\mathbf{r}, \mathbf{r}')}} \quad (14)$$

where  $P_1(\mathbf{r})$  is the local pressure which can be obtained from the EOS. Based on the Peng–Robinson EOS which is adopted in the current study,  $P_1(\mathbf{r})$  can be calculated as follows:

$$P_1(\mathbf{r}) = \frac{\rho_1(\mathbf{r})RT}{1 - b\rho_1(\mathbf{r})} - \frac{a\rho_1(\mathbf{r})^2 \varepsilon(T)}{1 + 2b\rho_1(\mathbf{r}) - b^2\rho_1(\mathbf{r})^2} \quad (15)$$

where  $\varepsilon(T) = [1 + (0.37464 + 1.54226\omega - 0.26992\omega^2)(1 - \sqrt{T/T_c})]^2$  with  $\omega$  as the acentric factor. The parameters  $a$ ,  $b$  are expressed as  $a = 0.45724R^2T_c^2/P_c$  and  $b = 0.0778RT_c/P_c$ , where  $T_c$  and  $P_c$  are the critical temperature and critical pressure, respectively. Following [Yuan and Schaefer \(2006\)](#), the following parameters are considered in the simulations of present study:  $\omega = 0.344$ ;  $a = 2/49$ ;  $b = 2/21$ ;  $R = 1$ .

The actual physical velocity  $\mathbf{U}$  is calculated by averaging the moment before and after the collision as follows:

$$\mathbf{U} = \frac{1}{\rho} \left( \sum_{\sigma} \rho_{\sigma} \mathbf{u}_{\sigma} + \frac{1}{2} \sum_{\sigma} \mathbf{F}_{\sigma} \right) \quad (16)$$

The evolution equation of the temperature distribution function  $h_{\alpha}(\mathbf{r}, t)$  is introduced to solve energy equation and can be written as follows:

$$h_{\alpha}(\mathbf{r} + \mathbf{e}_{\alpha} \delta_t, t + \delta_t) - h_{\alpha}(\mathbf{r}, t) = -\frac{1}{\tau_T} (h_{\alpha}(\mathbf{r}, t) - h_{\alpha}^{eq}(\mathbf{r}, t)) + \delta_t w_{\alpha} \phi \quad \alpha = 0, 1 \dots N \quad (17)$$

where  $\tau_T$  is the dimensionless relaxation time for temperature characterizing by thermal diffusivity. It can be calculated as  $\tau_T = 0.5 + 3\chi\delta_t / \delta_x^2$ , where  $\chi = \lambda / \rho c_v$  is the thermal diffusivity.  $\rho$ ,  $\lambda$ , and  $c_v$  represent total density, thermal conductivity and specific heat capacity, respectively.  $h_{\alpha}^{eq}(\mathbf{r}, t)$  denotes the corresponding equilibrium distribution function which is expressed as follows:

$$h_{\alpha}^{eq} = T w_{\alpha} \left( 1 + \frac{\mathbf{e}_{\alpha} \cdot \mathbf{U}}{c_s^2} + \frac{(\mathbf{e}_{\alpha} \cdot \mathbf{U})^2}{2c_s^4} - \frac{U^2}{2c_s^2} \right) \quad (18)$$

where  $T$  is the macro temperature which can be obtained as follows:

$$T = \sum_{\alpha} h_{\alpha} \quad (19)$$

The source term  $\phi$  in Eq. (17) represents the phase change effect on the temperature field. The source term proposed by [Gong and Cheng \(2012\)](#) is adopted in the present work which is expressed as follows:

$$\phi = T \left[ 1 - \frac{1}{\rho c_v} \left( \frac{\partial P}{\partial T} \right)_{\rho} \right] \nabla \cdot \mathbf{U} \quad (20)$$

where  $P$  can be obtained based on the EOS of multicomponent fluid which is given as follows ([Qiu and Wang, 2016](#)):

$$P = \rho c_s^2 + \frac{c_0}{2} \sum_{\sigma\bar{\sigma}} g_{\sigma\bar{\sigma}} \psi_{\sigma} \psi_{\bar{\sigma}} = (\rho_1 + \rho_2) c_s^2 + \frac{c_0}{2} (g_{11} \psi_1 \psi_1 + g_{12} \psi_1 \psi_2 + g_{21} \psi_2 \psi_1 + g_{22} \psi_2 \psi_2) \quad (21)$$

So, the source term  $\phi$  can be calculated after substitution of Eqs. (13), (14), (15) and (21) into Eq. (20), as follows:

$$\phi \approx T \left( 1 - \frac{1}{\rho c_v} \left( \frac{\rho_1 R}{1 - b\rho_1} + \frac{g_{12} \rho_1 \rho_2 R}{g_{11} (1 - b\rho_1) \psi_1} \right) \right) \nabla \cdot \mathbf{U} \quad (22)$$

The values  $\rho_2 = 1.0$ ,  $g_{11} = 0.1$  (or  $-0.1$ ), and  $g_{12} = 0.005$ ,  $g_{22} = 0$  are set according to [Liu \*et al.\* \(2018\)](#). As for multicomponent fluids,  $c_v$  is no longer a constant. It can be defined as the mass average of the specific heat capacity of each component which is expressed as follows:

$$c_v = 1/\rho \left( \sum_{\sigma} \rho_{\sigma} c_{v\sigma} \right) \quad (23)$$

## 2.2 Compressibility error analysis of the non-phase-change component

The MMPPCM can be utilized to simulate the vaporization of one liquid component in the multicomponent fluid. However, the compressibility

error restricts the model applicability in quantitative analysis of the foaming process. In the MMPPCM, the phase change components are compressible non-ideal fluids, while the non-phase-change component should be configured by an incompressible fluid with a constant density. However, the macro equations derived from the basic LBM model are compressible Navier-Stokes equations (Bespalko *et al.*, 2012). Especially in multicomponent models, the separation and diffusion processes between different components are determined based on the density, so variable density should be considered for each component in actual numerical calculations. Density changes of non-phase-change components leads to both compressibility errors and numerical instabilities. Particularly in the phase change process, vaporization of the phase change components causes a local pressure rise. This rapidly increases the pressure difference between components and changes the density of the non-phase-change components near the phase interface in the compressible LBM model. This reveals why the expansion rate and decay time in foaming process simulation can not be predicted exactly by the model. Local density variation of the non-phase-change components also causes numerical instability, which limits the density of these components. This is the reason why the non-phase-change components in most of the multicomponent multiphase models are considered as gas.

### 2.3 The improved model

One possible way to reduce the compressibility error of the non-phase-change component is to set  $g_{22} > 0$  in order to impose a repulsive force inside the component 2. However, it will increase the interparticle force at each lattice site in the computational domain, resulting in further instabilities. So, it is intended to improve the effective mass form of the component 2. In order to reduce the density change of the component 2 during the phase change process, the pressure difference  $\Delta P$  caused by density variation  $\Delta \rho$  in a multicomponent fluid should be increased. Liu *et al.* (2016) revealed that the effective mass form of the large-pressure-difference multicomponent model complies with the requirement. They analyzed the relationship between pressure difference and effective mass, and proposed a Sigmoid-like effective mass function to increase  $\Delta P$  near the interface between different components. This effective mass function is defined as follows:

$$\psi(\rho) = \frac{k}{1 + e^{i\rho+j}} - \frac{k}{1 + e^j} \quad (24)$$

where  $k$ ,  $i$  and  $j$  are adjustable parameters. It can be utilized to simulate multicomponent fluids with large pressure differences by appropriate tuning of parameters. According to Liu *et al.* (2016), the values  $k=0.75$ ,  $i=-6.0$ , and  $j=4.5$  are adopted in the following simulations. So, Eq. (13) can be rewritten as follows:

$$\psi_2(\mathbf{r}) = \frac{k}{1 + e^{i\rho_2(\mathbf{r})+j}} - \frac{k}{1 + e^j} \quad (25)$$

## 3. MODEL VERIFICATION

### 3.1 Verification of the MMPPCM model

Liu *et al.* (2018) simulated the phase change of a static droplet in binary fluids based on the MMPPCM. They analyzed the relationship between radius and density of droplet (or bubble) with time during the phase change process. In order to validate the present simulation, the similar problem is numerically solved and compared.

It should be mentioned that all variables in the current work are considered in terms of the lattice units. All the simulation settings are the same as those presented in Liu *et al.* (2018). Two types of components are initially considered in a  $200 \times 200$  lattice field in absence of gravitational effects, including a static liquid droplet of the component 1 at the center of the field surrounded by the component 2. The initial diameter and temperature of droplet are 40 and  $0.82T_c$ . The initial density of the component 1 is 7.0, which corresponds to saturated liquid density at the initial temperature. The initial temperature of the component 2 is set to  $2.0T_c$  to provide the required heat for phase change of the component 1. The initial density of the component 2 is 1.0. A non-equilibrium extrapolation scheme (Guo *et al.*, 2002) is used to maintain constant temperature and pressure over all boundaries. Temporal variation of the bubble radius as well as component density during phase change process is illustrated in Fig. 2. A quite good agreement can be observed between the simulation results of the present study and those of Liu *et al.* (2018).

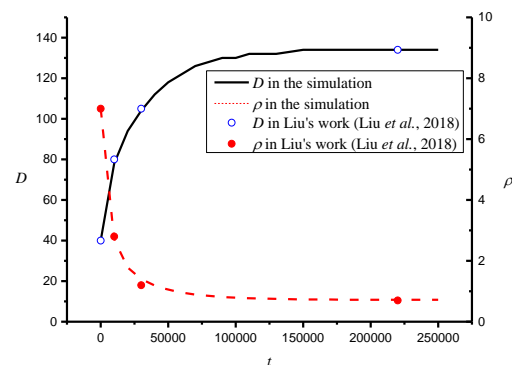


Fig. 2. Temporal variation of the bubble radius (D) as well as density ( $\rho$ ) during phase change process

### 3.2 Validation of the improved model

Since the effective mass function in the multicomponent model is modified and the interparticle force between the components is changed, the surface tension should be verified.

Verification is applied based on simulation of static droplets. Initially, a static droplet of the component 1 is placed at the center of a  $200 \times 200$  square gravity-free lattice field consisting of the component 2. The simulation is performed in the isothermal condition with the temperature of

0.82Tc. The density of the component 1 is set as the saturated liquid density at the corresponding temperature *T*. Heuristic scheme is utilized to apply periodic boundary conditions at all boundaries in the simulation. The surface tension  $\gamma$  can be obtained according to the Laplace law, which states the relationship between the pressure drop across the droplet interface ( $P_{in}-P_{out}$ ) and the droplet radius *r*. The Laplace law is expressed as follows:

$$\Delta P = P_{in} - P_{out} = \frac{\gamma}{r} \quad (26)$$

Several simulations are carried out based on droplets with different radii. The relationship between  $\Delta P$  and  $1/r$  as well as the curve obtained by linear fitting are shown in Fig. 3. The coefficient of determination of the fitted curve is 0.9998, which indicates that the surface tension obtained by the improved model is in good agreement with the Laplace law.

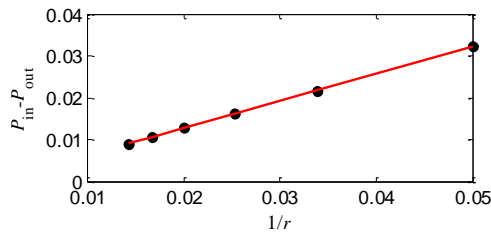


**Fig. 3. Relationship between  $P_{in}-P_{out}$  and  $1/r$  for static droplets in binary fluids.**

#### 4. RESULTS AND DISCUSSION

In this section, phase change process of static and moving fluids, and physical foaming process with orderly distributed droplets are simulated based on the improved model. The results are compared with the outcome of MMPPCM to confirm the simulation enhancement by the improved model. Physical foaming process with randomly distributed droplets and bubbles is finally simulated based on the improved model to show the model ability in numerical study of the actual foaming process.

##### 4.1 Phase change of a static droplet in binary fluids

In order to compare the compressibility errors obtained by the improved model and the MMPPCM, the phase change of a static droplet in binary fluids is also simulated by the improved model. The initial and boundary conditions are identical to those described in Section 3.1. Figure 4 shows the density field of the component 1 in phase change process. As can be observed, the droplet phase change originates gradually from the interface between two components and grows towards the droplet's interior region, which is similar to the results obtained by the MMPPCM. The droplet volume steadily expands continuously until reaching an equilibrium state based on the interior-exterior pressure difference of the bubble after phase change process. Finally, the flow field

involving the bubbles of the component 1 and the component 2 reaches a steady state condition at about 220 000 time steps.

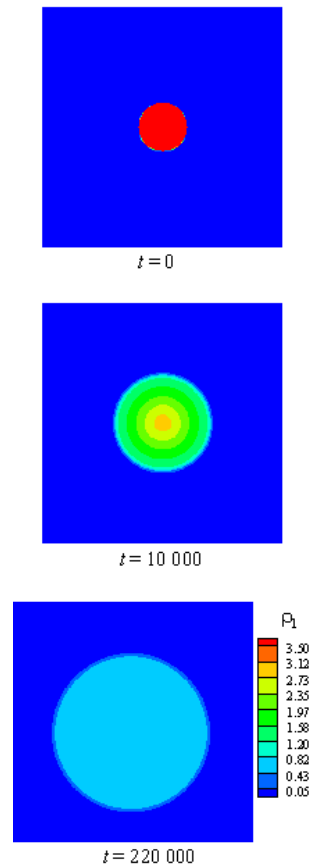


**Fig. 4. Temporal evolution of the density field of the component 1.**

Table 1 presents the density and bubble diameter of the component 1 after the phase change based on the improved model and the MMPPCM. Similar simulation results can be observed based on different models. The typical density ratio obtained by both models is about 10. This indicates that the change of effective mass form of the component 2 slightly affects the physical properties of the component 1 during the phase change process.

**Table 1. Density and bubble diameter of the component 1 after the phase change**

Simulation model	Density	Bubble diameter
MMPPCM	0.70	124
Improved model	0.69	123

Figure 5 shows the maximum density of the component 2 ( $\rho_{2max}$ ) over time during the phase change process based on the two models. Similar variation trend can be seen for the two models. Endothermic expansion of the component 1 leads to increase of the density of component 2 increases.

The highest value of  $\rho_{2max}$  for both of the models occurs at  $t = 20\,000$ . After this time,  $\rho_{2max}$  decreases and finally tends to a stable condition. However, the variation of  $\rho_{2max}$  in the simulation is significantly lower for the improved model. More specifically, the density variation of the component 2 based on the improved model is about 0.7 times of that of the MMPPCM at  $t = 20\,000$ . When the flow field is stable, this ratio can even be reduced to 0.65. This means that the improved model can improve the incompressibility of the non-phase-change component.

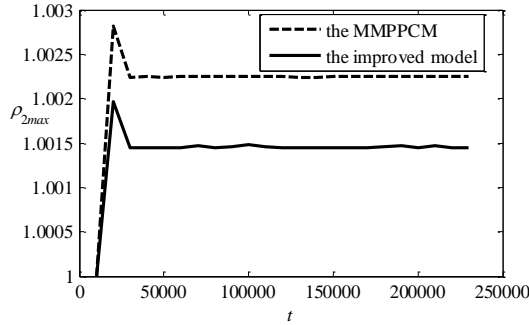


**Fig. 5. Variation of maximum density of component 2 ( $\rho_{2max}$ ) with time.**

Figure 6 presents temporal variation of the maximum velocity ( $U_{max}$ ) during the phase change process based on the two models. It can be observed that the highest value of  $U_{max}$  for both models occurs at about  $t = 20\,000$ , and then it gradually decreases towards a steady state condition. The stabilized condition of  $U_{max}$  corresponds to the maximum spurious velocity in the flow field. In comparison with the MMPPCM, the improved model can slightly reduce the maximum spurious velocity in the steady flow field after the phase change process. More importantly, the maximum value of  $U_{max}$  at  $t = 20\,000$  is reduced significantly. Therefore, utilization of the improved model leads to enhancement of computational stability. In summary, the improved model can enhance both the incompressibility of non-phase-change components and the numerical stability in simulation of the phase change process of a static droplet in binary fluid.

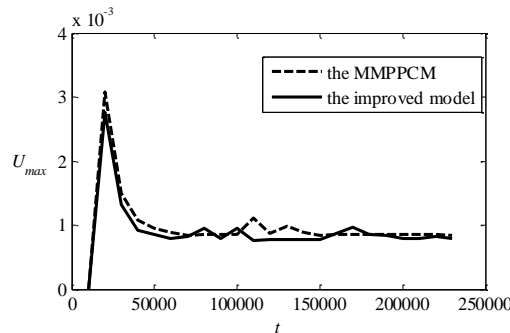


**Fig. 6. Variation of maximum velocity ( $U_{max}$ ) with time during the phase change process.**

#### 4.2 Phase change of a water droplet in binary fluid under gravitational effect

In order to evaluate properties of the improved model in moving fluid simulations, the phase change of water droplets in binary fluid is investigated under gravitational effect. The simulation results are compared with Liu *et al.* (2018) at the same settings. Initially, the  $200 \times 400$  lattice domain is occupied by the component 2 except for a  $10 \times 10$  square lattice area at the bottom center region of the overall domain which is occupied by the component 1. The bottom boundary of the computational domain is set as a constant temperature wall ( $T_{wall} = 2.0T_c$ ) with a constant velocity inlet ( $v = 0.05$ ) for the component 1, and other given data at the inlet include  $T_{inlet} = 0.82T_c$ ,  $\rho_{1inlet} = 7.0$  and  $\rho_{2inlet} = 0$ . The bounce-back and the non-equilibrium extrapolation schemes (Guo *et al.*, 2002) are adopted at the wall and the inlet for the density solution, respectively. And the non-equilibrium extrapolation scheme (Guo *et al.*, 2002) is adopted for the temperature solution. Periodic boundary conditions are applied at the right and left sides of the computational domain using the heuristic scheme for both the density and the temperature solutions. Constant pressure and constant temperature boundary conditions are applied at the top boundary, such that  $T_{top} = 2.0T_c$ ,  $\rho_{1top} = 0$  and  $\rho_{2top} = 1.0$ . The non-equilibrium extrapolation scheme (Guo *et al.*, 2002) is used for both the density and temperature solutions. The initial temperature of the components 1 and 2 are  $0.82T_c$  and  $2.0T_c$ , respectively. It should be noticed that the inlet is closed at  $t = 300$  to facilitate formation of droplets of the component 1. After this time, the bottom boundary condition is replaced with a constant temperature wall and the inlet boundary condition is removed. The gravitational effect of component 1 in the present simulation is imposed by a different approach than Eq. (10), such that it is expressed follows:

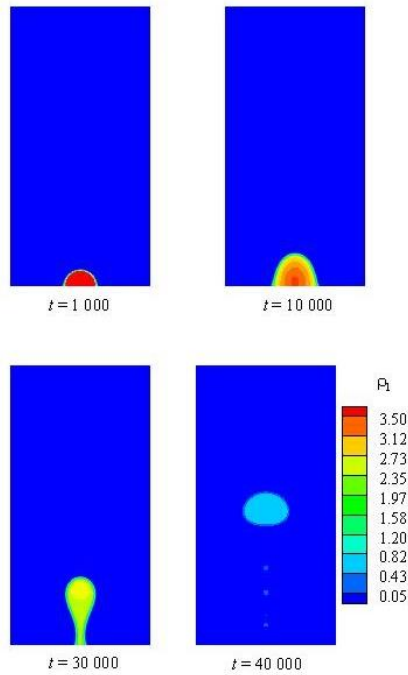
$$\mathbf{F}_{g,\sigma}(\mathbf{r}) = \begin{cases} 0, & \rho_1 < 0.1 \\ \mathbf{G} \cdot (\rho_\sigma(\mathbf{r}) - \rho_{\sigma,l}), & \text{else} \end{cases} \quad (27)$$

where  $\rho_{\sigma,l}$  denotes the saturated liquid density of component  $\sigma$  at the temperature  $0.82T_c$ .

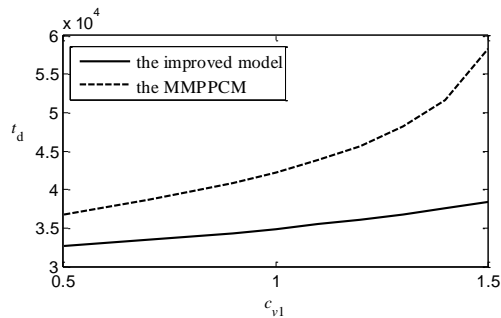
Figure 7 illustrates the density field of the component 1 obtained by the improved model with  $c_{v1} = c_{v2} = 1.0$ . It can be observed that the component 1 droplet gradually evolves into a bubble and rises from the bottom wall due to gravitational effect. Several simulations are performed with different values of  $c_{v1}$ .

Figure 8 presents the relationship between  $c_{v1}$  and the bubble departure time  $t_d$  for the two models. The departure time is the duration in which the bubble leaves the bottom wall. It can be considered as the time when there is a point  $\mathbf{r}$  with  $\rho_1(\mathbf{r}) < 0.1$  on the central axis of the inlet such that the ordinate of that point  $\mathbf{r}$  is less than the ordinate of the point corresponding to the maximum density of component 1. As can be seen from Fig. 8, the bubble departure time obtained by the improved

model increases non-linearly with the increase of  $c_{v1}$ , which is consistent with the simulation results of Liu *et al.* (2018). However, the departure time obtained by the improved model is shorter than that of the MMPPCM. This is because the improved model enhances the incompressibility of component 2, and due to the periodic conditions, the force between the components increases.



**Fig. 7. Contour plots of the density field of the component 1 at different times during phase change process**



**Fig. 8. The relationship between  $c_{v1}$  and the bubble departure time ( $t_d$ )**

### 4.3 Physical foaming process with orderly distributed droplets

The advantages of the improved model in the foaming process simulation are addressed by comparative study of the MMPPCM in multicomponent physical foaming process. Expansion rate and decay time are two quantitative indicators for the study of foam flow, which can be evaluated by variation of liquid level of the component 2 during the simulation. The simulation is performed in a  $200 \times 150$  computational domain. Initially, the region located above the line  $Y = 100$  is

occupied by the gaseous component 1, while the region below this line is filled by liquid fluids. Six droplets of the component 1 are uniformly dispersed in the lower fluid (component 2) as illustrated in Fig. 9 at  $t = 0$ . The initial temperature of droplets of the component 1 is  $0.82T_c$ , while the temperature of both the component 2 and the gaseous component 1 is  $2.0T_c$ . Configuration of the top boundary is identical to that applied in the previous simulation, while the other boundaries are considered as constant temperature walls with  $T = 2.0T_c$ . The bounce-back and the non-equilibrium extrapolation schemes (Guo *et al.* 2002) are applied for the density and the temperature solutions, respectively. Figure 9 illustrates the simulated physical foaming process based on the improved model. The blue area belongs to the component 2, while the red spots and the green region correspond to the droplets and bubbles of the component 1, respectively. It can be seen that as droplets of the component 1 vaporize, the multicomponent fluid expands and liquid level of the component 2 rises initially. When the bubbles reach to the liquid upper surface and burst, the liquid level descends.

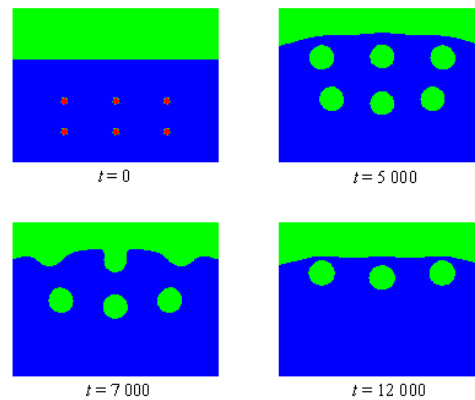


**Fig. 9. Temporal evolution of the physical foaming process**

Figure 10 presents temporal variation of the averaged the average liquid level height of the component 2 during the foaming process based on the two models. Three different contents of the component 1 are considered (with the initial radius  $r_1$  of droplets as 3, 5 and 6). The stepwise descend of the level is due to the collapse of large bubbles as mentioned by Jenkins (2000). Comparison of three parts of Fig. 10 indicates that by increase of the content of the component 1 increases, whereas the level decays faster. It can also be observed that the maximum height of the liquid level of component 2 is greater for the improved model simulation. In contrast, the minimum heights obtained by the two models are approximately identical, because the expansion rate obtained by the improved model is more significant. This is exactly due to effect of the improved model on reduction of the compressibility error in comparison with the MMPPCM.

Table 2 presents the variation of liquid level during the foaming process in each simulation. The ratio of the liquid level variation of the improved model to

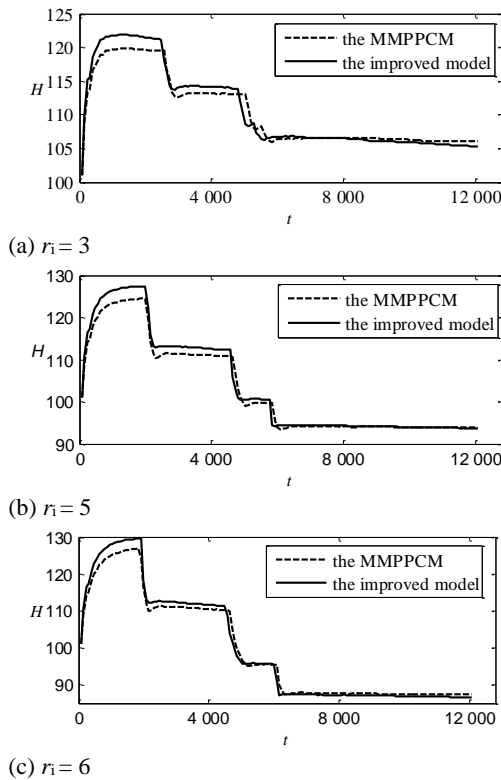


**Fig. 10. Temporal variation of the averaged liquid level height of the component 2**

**Table 2 The variation of liquid level during the foaming process**

the variation of liquid level	$r_1 = 3$	$r_1 = 5$	$r_1 = 6$
The improved model	16.7	33.5	42.9
The MMPPCM	13.7	30.7	39.6
Variation ratio	1.22	1.09	1.08

that of the MMPPCM model is about 1.1 ~ 1.2. This indicates that 10% ~ 20% of compressibility error is corrected by the improved model.

As for the decay time, it can be seen from Fig. 10 that the required time to return to the minimum liquid level is slightly shorter for the improved model in all three sets of comparative simulations. In other words, bubbles rise faster when the improved model is implemented in simulations. The reason for this phenomenon is the same as that discussed in the previous simulation case which is the increase of incompressibility of the component 2. Overall, it can be seen from the simulations that the improved model is more suitable for quantitative analysis of the physical foaming process.

#### 4.4 Physical foaming process with randomly distributed droplets and bubbles

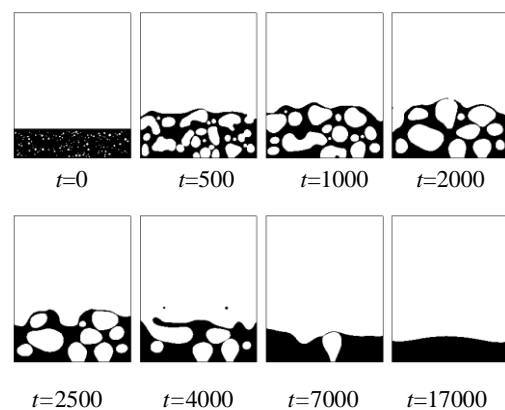
In the previous case, droplets of the component 1 were arranged in an ordered manner during initialization stage. However, in the actual foaming process, distribution of the component 1 in the

component 2 is often disordered, and the component 1 may exist in both gas and liquid phases. Content of the component 1 is the only adjustable feature. In this case, the foaming process with randomly distributed droplets and bubbles is simulated. The computational domain consists of  $400 \times 500$  cells, and the simulation settings are the same as the previous case except for the initial distribution of component 1. According to Hailesilassie (2016), the relationship between the number of droplets (bubbles)  $f(x)$  and their size is represented by the following exponential function:

$$f(x) = me^{-0.05x} \quad (28)$$

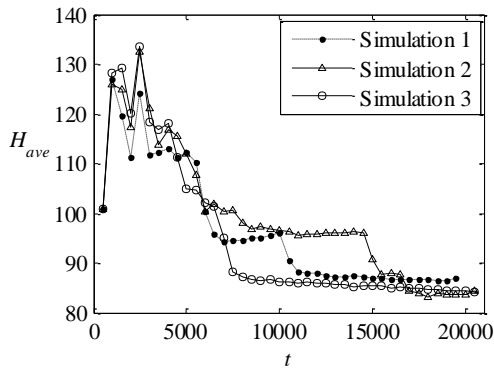
where  $x$  denotes the area of a single droplet (bubble) and  $m$  represents the distribution parameter, which can be obtained based on the total area for a certain radius condition. The radius of droplets (bubbles) of the component 1 is set in the range of 1-4 in this case. The number of droplets (bubbles) with different radii is obtained based on the total content of the component 1 and using Eq. (28). A random distribution algorithm is utilized to ensure that the droplets (bubbles) of the component 1 do not coincide with each other during the initialization stage. Initially, 80% of the component 1 is considered as the liquid phase, and the rest is the gas phase. Based on this configuration, the foaming process with four contents of the component 1, i.e. 2%, 3%, 4% and 5% is simulated (3 simulations under each condition).

Figure 11 illustrates temporal evolution of the foaming process when the content of the component 1 is 4%. The black area in this figure is the component 2, and the white area corresponds to the component 1 with the liquid or gas phases. Merging and breaking of the bubbles of component 1 as well as variation of the liquid level height of the component 2 can be clearly observed during the foaming process.

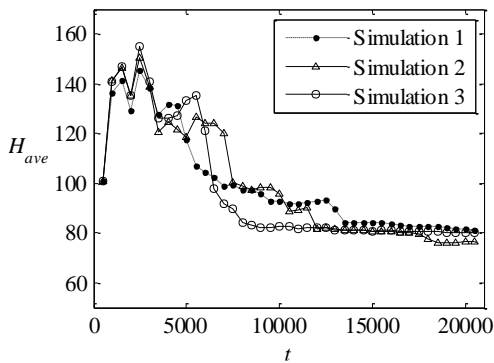


**Fig. 11. Temporal evolution of the physical foaming process with randomly distributed droplets and bubbles (the content of the component 1 is 4%)**

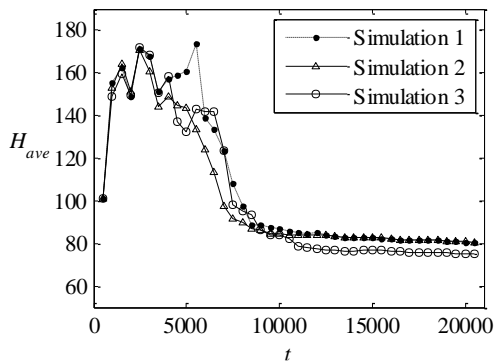
Figure 12 presents temporal variation of the averaged liquid level of component 2 for different contents of component 1 during the physical



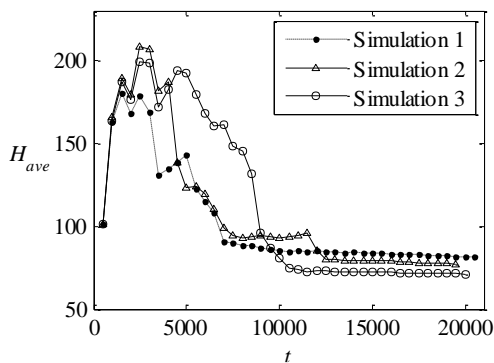
(a) 2%



(b) 3%



(c) 4%



(d) 5%

**Fig. 12. Temporal variation of the averaged liquid level of component 2 for four different contents of component 1 during the physical foaming process.**

foaming process. By increase of the content of the component 1, the foam expansion rate increases and the decay time shortens. These trends are consistent with those observed in the previous case, and they are also consistent with the effect of water content on foamed asphalt in terms of expansion rate and half-life (Jenkins, 2000). It is also evident that the expansion rate obtained from the three simulations with similar conditions is basically the same, while the decay time changes significantly under certain conditions (such as the case with 5% content for the component 1). This is explained by the fact that the initial distribution of the component 1 affects the foam stability. If the distribution is too concentrated, large bubbles are generated easily during the initial foaming process, and this accelerates the foam attenuation (Jenkins, 2000). Therefore, in order to conduct a quantitative comparison with the actual foaming process, the initial bubble distribution must be accurately described.

### 5. CONCLUSION

In the present study, we propose an improved multicomponent multiphase pseudopotential model was proposed for physical foaming simulations. It was a modification of the MMPPCM by introducing an effective mass form of the high-pressure-difference multicomponent model in the non-phase-change component. The proposed model improved the incompressibility of non-phase-change component in multicomponent fluid, and reduced the errors of expansion rate and decay time in the physical foaming simulations. The improved model was verified based on simulation of a static droplet in binary fluids. It was utilized to simulate the phase change process of static and moving fluids, as well as the physical foaming process. According to the results, about 10% ~ 20% reduction of compressibility error was observed for the improved model as compared with the MMPPCM. The improved model also enhanced computational stability of phase change simulation of the static droplets. The present study simulations were conducted based on 2D foaming process, 3D simulation and quantitative comparison of the results with the actual foaming process will be presented in our future research.

### ACKNOWLEDGEMENT

The authors are grateful to the financial support from Key R & D project of Shandong Province under Grant No. 2020CXGC010312 and the expert linguistic services provided by EditSprings (<https://www.editsprings.cn/>).

### REFERENCES

Aliu, O., H. Sakidin, J. Foroozesh and N. Yahya (2020). Lattice Boltzmann application to nanofluids dynamics-A review. *Journal of Molecular Liquids* 300, 112284.

Ataei, M., V. Shaayegan, F. Costa, S. Han, C. B. Park and Busmann M. (2021). LBfoam: An

- open-source software package for the simulation of foaming using the Lattice Boltzmann Method. *Computer Physics Communications* 259, 107698.
- Bespalko, D., A. Pollard and M. Uddin (2012). Analysis of the pressure fluctuations from an LBM simulation of turbulent channel flow. *Computers & fluids* 54, 143-146.
- Fogliatto, E. O., A. Clausse and F. E. Teruel (2019). Simulation of phase separation in a Van der Waals fluid under gravitational force with Lattice Boltzmann method. *International Journal of Numerical Methods for Heat & Fluid Flow* 29(9), 3095-3109.
- Gong, S. and P. Cheng (2012). A lattice Boltzmann method for simulation of liquid–vapor phase-change heat transfer. *International Journal of Heat and Mass Transfer* 55(17-18), 4923-4927.
- Gong, S. P. and Cheng (2013). Lattice Boltzmann simulation of periodic bubble nucleation, growth and departure from a heated surface in pool boiling. *International Journal of Heat and Mass Transfer* 64, 122-132.
- Gong, S. and P. Cheng (2015). Lattice Boltzmann simulations for surface wettability effects in saturated pool boiling heat transfer. *International Journal of Heat and Mass Transfer* 85, 635-646.
- Gunstensen, A. K., D. H. Rothman, S. Zaleski and G. Zanetti (1991). Lattice Boltzmann model of immiscible fluids. *Physical Review A* 43(8), 4320.
- Guo, Z. L., C. G. Zheng and B. C. Shi (2002). Non-equilibrium extrapolation method for velocity and pressure boundary conditions in the lattice Boltzmann method. *Chinese Physics* 11(4), 0366-0374.
- Hailesilassie, B. (2016). *Morphology Characterization of Foam Bitumen and Modeling for Low Temperature Asphalt Concrete*. Ph. D. thesis, KTH Royal Institute of Technology, Stockholm, Sweden.
- Házi, G. and A. Márkus (2009). On the bubble departure diameter and release frequency based on numerical simulation results. *International Journal of Heat and Mass Transfer* 52(5-6), 1472-1480.
- Iwański, M., G. Mazurek, P. Buczyński and J. Zapala-Sławeta (2021). Multidimensional analysis of foaming process impact on 50/70 bitumen ageing. *Construction and Building Materials* 266, 121231.
- Jenkins, K. J. (2000). *Mix design considerations for cold and half-warm bituminous mixes with emphasis of foamed bitumen*. Ph. D. thesis, Stellenbosch University, Stellenbosch, South Africa.
- Jourabian, M., M. Farhadi and A. A. R. Darzi (2012). Lattice Boltzmann investigation for enhancing the thermal conductivity of ice using Al<sub>2</sub>O<sub>3</sub> porous matrix. *International Journal of Computational Fluid Dynamics* 26(9-10), 451-462.
- Körner, C., M. Thies, T. Hofmann, N. Thürey and U. Rüde (2005). Lattice Boltzmann model for free surface flow for modeling foaming. *Journal of Statistical Physics* 121(1), 179-196.
- Kupershtokh, A. L., D. A. Medvedev and D. I. Karpov (2009). On equations of state in a lattice Boltzmann method. *Computers & Mathematics with Applications* 58(5), 965-974.
- Li, M., C. Huber, Y. Mu and W. Tao (2017). “Lattice Boltzmann simulation of condensation in the presence of noncondensable gas”, *International Journal of Heat and Mass Transfer* 109, 1004-1013.
- Li, N., W. Tang, X. Yu, H. Zhan, H. Ma, G. Ding and Y. Zhang (2020). Investigation of Moisture Dissipation of Water-foamed Asphalt and Its Influence on the Viscosity. *Materials* 13(23), 5325.
- Liu, F. M. and A. L. Wang (2018). Numerical Investigation on Physical Foaming and Decay Process Using Multicomponent Thermal Lattice Boltzmann Model. *MATEC Web of conference* 237, 02003.
- Liu, F. M., A. L. Wang and Z. S. Fu (2018). Multicomponent lattice Boltzmann model for simulation of phase change with heat transfer. *The Canadian Journal of Chemical Engineering* 96(9), 2035-2042.
- Liu, F. M., A. L. Wang, R. F. Qiu and T. Jiang (2016). Improved lattice Boltzmann model for multi-component diffusion flow with large pressure difference. *International Journal of Modern Physics C* 27(11), 1650130.
- Lu, S., J. Zhu, D. Gao, W. Chen and X. Li (2020). Lattice Boltzmann simulation for natural convection of supercritical CO<sub>2</sub> in an inclined square cavity. *International Journal of Numerical Methods for Heat and Fluid Flow* 30(7), 3635-3652.
- Márkus, A. and G. Házi (2011). Simulation of evaporation by an extension of the pseudopotential lattice Boltzmann method: A quantitative analysis. *Physical Review E* 83(4), 046705.
- Martys, N. S. and H. Chen (1996). Simulation of multicomponent fluids in complex three-dimensional geometries by the lattice Boltzmann method. *Physical Review E* 53(1), 743.
- Petersen, K. J. and J. R. Brinkerhoff (2021). On the lattice Boltzmann method and its application to turbulent, multiphase flows of various fluids including cryogenics: A review. *Physics of Fluids* 33(4), 041302.

- Qiu, R. F. and A. L. Wang (2016). Numerical investigation of two-component jet flow with heat transfer in a channel by lattice Boltzmann method. *Computers & Fluids* 138, 1-8.
- Sedahmed, M., R. C. V. Coelho and H. A. Warda (2022). An improved multicomponent pseudopotential lattice Boltzmann method for immiscible fluid displacement in porous media. *Physics of Fluids* 34(2), 023102.
- Shan, X. and H. Chen (1993). Lattice Boltzmann model for simulating flows with multiple phases and components. *Physical Review E* 47(3), 1815.
- Swift, M. R., E. Orlandini, W. R. Osborn and J. M. Yeomans (1996). Lattice Boltzmann simulations of liquid-gas and binary fluid systems. *Physical Review E* 54(5), 5041.
- Xing, Z. B., X. Han, H. Ke, Q. G. Zhang, Z. Zhang, H. Xu and F. Wang (2021). Multi-phase lattice Boltzmann (LB) simulation for convective transport of nanofluids in porous structures with phase interactions. *International Journal of Numerical Methods for Heat & Fluid Flow* 31(8), 2754-2788.
- Yuan, P. and L. Schaefer (2006). Equations of state in a lattice Boltzmann model. *Physics of Fluids* 18(4), 042101.
- Zhang, C., P. Cheng and W. J. Minkowycz (2017). Lattice Boltzmann simulation of forced condensation flow on a horizontal cold surface in the presence of a non-condensable gas. *International Journal of Heat and Mass Transfer* 115, 500-512.
- Zhang, Y., Y. Huang, M. Xu, Q. Wan, W. Li and Y. Tian (2020). Flow and heat transfer simulation in a wall-driven porous cavity with internal heat source by multiple-relaxation time lattice Boltzmann method (MRT-LBM). *Applied Thermal Engineering* 173, 115209.
- Zheng, S., F. Eimann, C. Philipp, T. Fieback and U. Gross (2019). Single droplet condensation in presence of non-condensable gas by a multi-component multi-phase thermal lattice Boltzmann model. *International Journal of Heat and Mass Transfer* 139, 254-268.